

# Process and Drying Behavior Toward Higher Drying Rates of Hard Carbon Anodes for Sodium-Ion Batteries with Different Particle Sizes: An Experimental Study in Comparison to Graphite for Lithium-Ion-Batteries

Julian Klemens,\* Luca Schneider, David Burger, Nadine Zimmerer, Marcus Müller, Werner Bauer, Helmut Ehrenberg, Philip Scharfer, and Wilhelm Schabel

Sodium-ion batteries are considered to be one of the most promising postlithium batteries on the verge of commercialization. The electrode processing is expected to be similar to lithium-ion batteries. However, the producibility and material processing challenges of potential electrode materials for anodes and cathodes are poorly understood. For industrial electrode production, a deep understanding of the processing of electrode materials with different particle morphologies is of great importance. In particular, the correlation between the process conditions and the electrode properties needs to be investigated further to understand the complex interactions between the battery slurry materials, the binder system, the drying process, and the microstructure formation. One promising anode material is hard carbon. The water-based processing of hard carbon slurries presented in this article shows that the drying behavior is strongly interconnected with the particle size and particle interactions in the drying electrode. This study shows that all the hard carbons investigated do not exhibit binder migration at moderate drying rates. Even at very high drying rates ( $9 \text{ g m}^{-2} \text{ s}^{-1}$ , 12 s drying time), an increase in adhesion force of up to 39% is observed for comparatively smaller particles compared to the adhesion force at lower drying rate.

## 1. Introduction

Lithium-ion batteries (LIB) and sodium-ion batteries (SIB) are both based on similar intercalation/insertion electrodes of the respective alkali ions into the active materials during charging and discharging.<sup>[1]</sup> Due to the larger and heavier sodium (Na) ion, a lower gravimetric and as well volumetric capacity than with lithium can be achieved.<sup>[2,3]</sup> However, given the resource availability of active materials from sustainable raw materials, at potentially low cost, SIB is one of the most promising post-Li batteries for widespread commercialization in the coming years.<sup>[4–6]</sup> Electrode processing of materials for SIB is expected to be very similar to the processing of LIB materials. However, the producibility and material processing challenges of potential electrode materials for anodes and cathodes are poorly investigated.

Unlike for the LIB, graphite cannot be recommended as anode material for the SIB, because the formation of a Na–graphite–intercalation compound is energetically unfavorable and has a very low capacity.<sup>[7–10]</sup> Instead, hard carbon (HC) is considered to be a promising anode active material with good electrochemical performance for alkali-metal-ion batteries, such as SIBs.<sup>[8]</sup> The low material costs, the fact that HC can be produced from sustainable raw materials, and the low electrode potential are advantageous for the use of HC as an anode material for SIB.<sup>[11,12]</sup> However, high capacity losses in the first cycles and at high current rates are still challenging. The performance characteristics of HC active materials, which result from different synthesis methods, are different.<sup>[8]</sup> The selected precursor and the carbonization conditions, namely, the carbonization temperature, influence the nongraphitic structure of the HC produced and thus, its properties.<sup>[2,8,10]</sup> The non graphitic structure of the HC offers various areas where Na ions can be deposited. These include especially the regions between the graphite-like domains consisting of micropores and defect sites. Various models describing the storage mechanism, which are controversially discussed, can be found in the literature.<sup>[2,10,13,14]</sup>

J. Klemens, D. Burger, N. Zimmerer, P. Scharfer, W. Schabel  
Thin Film Technology (TFT)  
Karlsruhe Institute of Technology (KIT)  
Straße am Forum 7, D-76131 Karlsruhe, Germany  
E-mail: julian.klemens@kit.edu

L. Schneider, M. Müller, W. Bauer, H. Ehrenberg  
Institute for Applied Materials (IAM)  
Karlsruhe Institute of Technology (KIT)  
Hermann-von-Helmholtz-Platz 1, 76344 Eggenstein-Leopoldshafen,  
Germany

 The ORCID identification number(s) for the author(s) of this article can be found under <https://doi.org/10.1002/ente.202300338>.

© 2023 The Authors. Energy Technology published by Wiley-VCH GmbH. This is an open access article under the terms of the Creative Commons Attribution License, which permits use, distribution and reproduction in any medium, provided the original work is properly cited.

DOI: 10.1002/ente.202300338

Furthermore, the microstructure of the produced electrodes and the particle morphology used have an influence on the mechanical, electrical, and electrochemical properties of battery electrodes,<sup>[15–17]</sup> which have not been investigated for HC electrodes in the literature so far. The microstructure is formed during drying of the applied electrode slurry on the current collector and the properties of the electrodes depend on the drying conditions. Especially at industrially relevant drying rates ( $1.5 \text{ g m}^{-2} \text{ s}^{-1}$  and higher),<sup>[18]</sup> the homogeneity of the binder distribution can be affected negatively. Nevertheless, high drying rates are aimed for, since the drying time still is a limiting factor in the production of battery electrodes.<sup>[19]</sup>

During the electrode drying process, the porous microstructure of the electrode is developed in different stages.<sup>[15,17,20–22]</sup> When solvent evaporates the applied film shrinks, causing the particles in the drying slurry to approach each other. The final porosity of the electrode is reached as soon as the particles do not approach any further. By the end of the film shrinkage, at the latest, a capillary network with solvent-filled pores has formed which subsequently empties. A challenge in the processing of battery electrodes is the occurrence of binder migration due to capillary transport. An increasing drying rate leads to the depletion of binder near the current collector and thus, to a decreasing adhesion force. The accumulation of the migrated binder at the upper surface (near the separator) of the electrode leads to an increased ionic transport resistance as a result of clogging of the pores.<sup>[15,16,18,21–28]</sup> In former studies it has been shown for graphite anodes that increasing the drying rate by either increasing the drying temperature or by increasing the heat and mass transfer coefficients by the applied air flow conditions has significantly different effects on the properties of the electrodes.<sup>[18]</sup> Increasing the drying rate by a higher drying temperature leads to less reduction of the adhesion strength than by increasing the heat and mass transfer coefficient.<sup>[18]</sup> This is important to consider for the choice of drying processes on an industrial scale.

Investigations of the microstructure formation of graphite anodes with the thickener carboxymethyl cellulose (CMC) and styrene-butadiene-rubber (SBR) as adhesion agent show that the polymeric CMC forms a network in the dried electrode.<sup>[16,29,30]</sup> This network is influenced by the interactions between the CMC, SBR, and the particles, which depend on the surface properties of the active materials and conductive additive.<sup>[31]</sup> For example, the degree of substitution of the hydrogen in the hydroxyl groups by a carboxymethyl group and the molecular weight influence the adsorption behavior of CMC on graphite.<sup>[32]</sup> It is hypothesized that the interactions between the CMC functional groups and the particle surface influence the formation of specific bonds during drying.<sup>[33]</sup> In a previous study on the rheology of graphite slurries, it could be shown that when the CMC concentration in the slurry is increased, the adsorbed amount of CMC on the graphite particles also increases.<sup>[34]</sup> Thus, the SBR is primarily part of the polymer-network structure and less of the SBR adsorbs on the graphite surface. The effect of a stronger binding of SBR in the CMC network was previously studied by increasing the drying rate for different graphite particles.<sup>[16]</sup> Based on cryogenic broad ion beam scanning electron microscopy (cryo-BIB-SEM) images, it was assumed that on the one hand the CMC can be stronger bound to the graphite particles and on the other hand the SBR binder adheres to the fixed

CMC,<sup>[16,18,34]</sup> and thus, migrates less or not at all during drying.<sup>[16]</sup> Mixing with a kneader, and thus, a grinding of the graphite particles and also the grinding of conductive carbon black or using smaller spherical graphite particles, it could be shown that a lower or no migration of the binder takes place.<sup>[16]</sup> The higher number of particles is expected to lead to more contact sites between the CMC/SBR network and the particles. In addition to the increasing number of binding sites, the surface of the spherical graphite, for example, is thought to be responsible for a higher adhesion force by possessing more hydroxyl groups to further promote the fixation of carboxyl groups of the polymer on the graphite surface.<sup>[16]</sup> This shows that the mechanistic understanding of microstructure evolution during drying is a complex task that requires the investigation of various parameters, such as the influence of particle morphology on the (drying) process–structure formation relation under defined process conditions. It is not yet known from the literature how HC particles behave compared to graphite during electrode fabrication and regarding binder migration at higher drying rates.

In this article, the processing of HC with different particle sizes for SIB anodes at industrially relevant drying conditions and even beyond was investigated using a specialized drying apparatus.<sup>[23]</sup> First, the particle properties and the flow behavior of water-based slurries were investigated. Then HC electrodes were cast and dried at increasing drying rates at different isothermal drying temperatures and film temperatures. The microstructure formation and binder migration of different HC slurries was investigated and the adhesion force of the electrodes was evaluated as a function of the drying conditions. The study also integrates measurements of adhesion force from aqueous graphite anodes obtained from a previously published work<sup>[18]</sup> to compare the influences at the same electrode composition, solid content, and drying conditions.

In all experiments, the drying rate was chosen as the fundamental comparative variable. Thus, the drying conditions used in this study can be assigned to any other dryer, which can be adjusted to generate identical drying rates and film temperatures. In addition, the transport properties in HC electrodes are investigated by impedance measurements under blocking conditions to study the effect of binder migration on the ionic transport resistance and the electrical tortuosity derived from it. This is investigated for HC electrodes that show binder migration with increasing drying rate and for HC electrodes that do not show binder migration.

## 2. Results and Discussion

### 2.1. HC Particle Properties

Three different HC materials with different particle properties were selected for the investigations in this study. **Figure 1** shows SEM images of the three HC powders used in this study. For comparison, an SEM image of graphite particles is shown in **Figure S1**, Supporting Information.

The HC particles have an irregular, granular shape, and differ in particle size. Nonspherical graphite, on the other hand, which is often used in the literature, shows a flake-like particle shape with a larger average particle size than all HC. The average

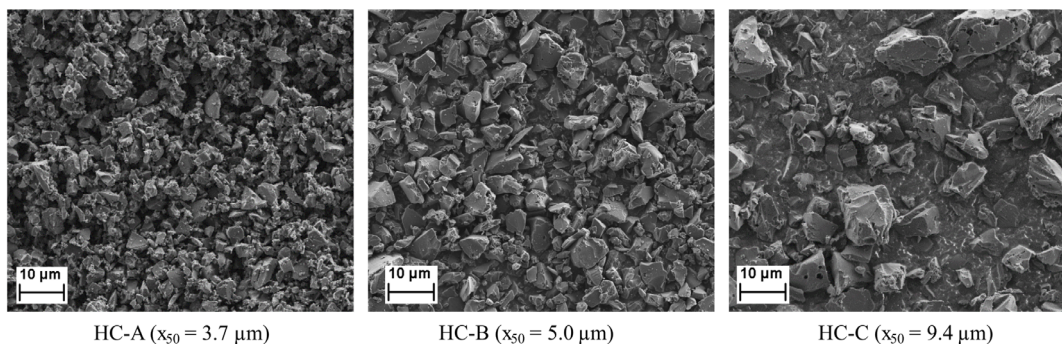


**Figure 1.** SEM images of the three different HC powders. The HC particles have an irregular, granular shape and differ in their average particle size. In Figure S1, Supporting Information, an SEM image of a non-spherical (flake-like) graphite with the average particle size of 18.4  $\mu\text{m}$  is shown for comparison.

**Table 1.** Overview of the particle properties of the investigated HC materials.

Name	Average particle diameter ( $x_{50}$ [ $\mu\text{m}$ ])	Specific surface area (BET [ $\text{m}^2 \text{g}^{-1}$ ])	Material density [ $\text{kg m}^{-3}$ ]
HC-A	3.7	$9.83 \pm 0.12$	$1949 \pm 3$
HC-B	5.0	$4.99 \pm 0.05$	$2069 \pm 2$
HC-C	9.4	$3.46 \pm 0.04$	$2062 \pm 2$
Graphite <sup>[16]</sup>	18.4	2.7	2260

particle diameter, the specific surface area Brunauer, Emmett, and Teller (BET), and the density (measured by gas pycnometry) of the particles are shown in **Table 1**.

The specific surface area of a non-spherical, flake-like graphite from the literature is given as  $2.7 \text{ m}^2 \text{g}^{-1}$  ( $x_{50} = 18.4 \mu\text{m}$ ).<sup>[16]</sup> As the average particle diameter increases, the specific surface area decreases. The influence of solid–electrolyte interphase (SEI) formation on the electrochemical performance for graphite with different particle sizes is discussed in the literature.<sup>[16]</sup> Due to a higher active surface area, the performance of the cell is affected by nonreversible lithium loss during the formation of the SEI.<sup>[16]</sup> The smaller particle size of HC-A particles leads as well to a higher capacity loss due to SEI formation compared to HC-C particles. In turn, the larger particles show a higher overpotential. More details on the influence of particle size on the voltage profile during charging and discharging of HC electrodes in half cells against sodium metal can be found in the Supporting Information.

The HC particles show a fairly similar density and density of the graphite is about 10 % higher than for HC, which affects the volume fractions in the slurry (Section 2.2).

## 2.2. Slurry Flow Behavior

To compare the different HC particles with graphite, the slurries were produced with the same solid content of 43 wt% and using the identical manufacturing procedure and mixing parameters (Section 4.1). **Figure 2** shows the results of the viscosity measurements of the HC slurries with the different HC particles for SIB anodes in comparison to the graphite slurry for LIB anodes as a

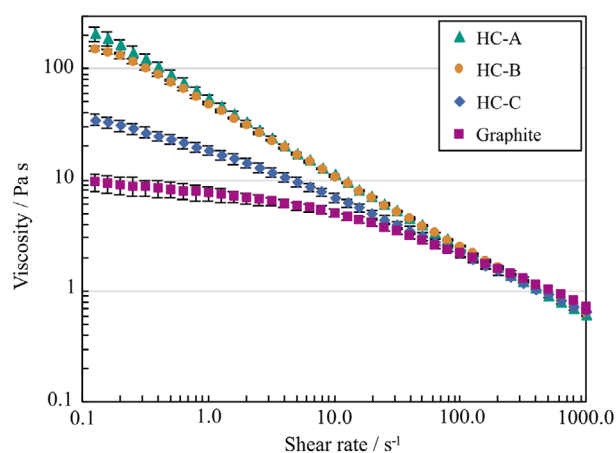


**Figure 2.** Viscosity as a function of the shear rate measured at 25 °C for the HC slurries for SIB electrodes with different particle sizes (HC-A  $x_{50} = 3.7 \mu\text{m}$ , HC-B  $x_{50} = 5.0 \mu\text{m}$ , HC-C  $x_{50} = 9.4 \mu\text{m}$ ) and the graphite ( $x_{50} = 18.4 \mu\text{m}$ ) slurry for LIB anodes with the same composition and water content as well as the identical slurry mixing procedure (see Experimental Section). The HC slurries show higher viscosities by a factor of 4–23 (HC-C and HC-A) than the graphite slurry in the low-shear region of  $0.1 \text{ s}^{-1}$ . Toward higher shear rates ( $>50 \text{ s}^{-1}$ ) the viscosity of all slurries aligns toward liquid properties and is almost the same.

function of the shear rate in a double-logarithmic plot. Information on viscosity measurement is given in Section 4.1.

At lower shear rates, the HC-A slurry with the smallest particle size shows the highest viscosity and the graphite slurry with the largest particle size shows the lowest viscosity. This corresponds to the anticipated behavior that due to more particle–particle interactions and more particle–CMC/SBR interactions in a system with smaller particle size and higher specific surface area, the viscosity increases.<sup>[35]</sup> In addition to the effect of particle size, the volume fraction of HC is increased by about 9% compared to graphite in the slurry due to its lower density (Table 1). More information about the calculation of the volume fractions and the comparison is given in Table S2, Supporting Information.

The viscosity of the HC slurries differs especially in the low-shear-rate range and up to  $\approx 100 \text{ s}^{-1}$ . Thereby, the viscosities at low shear rate ( $0.1 \text{ s}^{-1}$ ) of HC-A and HC-B with  $228 \pm 37 \text{ Pa s}$  and  $158 \pm 9 \text{ Pa s}$  are more similar than the viscosity of HC-C

with  $37 \pm 4$  Pa s. This is to be expected since the mean particle sizes of HC-A and HC-B are closer to each other. In addition, HC-C shows a broader particle size distribution (Figure S2, Supporting Information) compared to HC-A and HC-B, which tends to result in a lower viscosity in the low-shear-rate range. Another difference of HC-A and HC-B compared to HC-C and graphite could be the stability behavior of the slurries. This has been investigated by frequency sweep measurements shown in the Figure S3, Supporting Information. HC-A and HC-B slurries show a “gel-like” behavior, which results in a comparatively higher viscosity in the low-shear region,<sup>[24,35]</sup> whereas the HC-C and the graphite slurry<sup>[16]</sup> show a “liquid-like” behavior. Gel-like behavior was also observed for graphite slurries prepared in a kneader.<sup>[16]</sup> High shear forces in the kneader during mixing partially reduce the size of the graphite, resulting in a fraction of small particles and also a deagglomeration of the carbon black, leading to a gel-like behavior due to more pronounced particle–particle interaction and more particle–polymer contact points between the CMC and the particles.<sup>[16]</sup> HC-A and HC-B compared to HC-C and graphite could lead to stronger bridging of the CMC network with the particles during slurry production, also resulting in a gel-like behavior.

Note that slurries with higher viscosity at low shear rate and shear thinning behavior help to form lower side edges and, thus, less defects in the slot-die coating process.<sup>[36]</sup> This reduces the reject rate during electrode production.<sup>[37–39]</sup>

Since the same solid content and the same electrode composition with the same CMC amount was adjusted, all three HC slurries for SIB and the graphite slurry for LIB show the same behavior for the viscosity at a shear rate above  $100 \text{ s}^{-1}$ . In the slot-die-coating process at state-of-the-art industrial coating speeds, typical shear rates in the coating gap are above  $400 \text{ s}^{-1}$ .<sup>[37,40]</sup> It is assumed that the processability, in particular toward faster industrial coating speeds, will be similar for all investigated slurries and the coating equipment for LIB anodes at pilot and industrial coating plants can be used for HC slurries for SIB without major changes or investments.

Based on the viscosity behavior and the findings from the literature, it is expected that stronger bridging of the CMC network may lead to reduced binder migration for the HC-A and HC-B particles. Assuming that the SBR binder is attracted to the CMC,<sup>[34]</sup> a lower mobility of the SBR during drying can be expected as a result.<sup>[16]</sup> Adhesion force measurements and impedance spectroscopy measurements for electrodes produced at different increasing drying rates were used to address these hypotheses (Section 2.4 and 2.5).

### 2.3. Microstructure of HC Electrodes

To characterize the microstructure by the development of the adhesion force of different HC for increasing drying rate, the electrodes are manufactured under quasi-isothermal drying conditions in a specialized apparatus.<sup>[18,21,23]</sup> This means that the temperature of the temperature-controlled plate and the drying air are set to the temperature that a drying slurry would take as wet bulb temperature if it was dried in a convective roll-to-roll dryer.<sup>[18]</sup> In this way, the different electrodes can be produced under identical conditions.

**Table 2.** Dry film thickness, area weight, electrode density, and electrode porosity of noncalendered HC electrodes with different particle sizes. For comparison, the data for a graphite anode are also given.

Name	Dry film thickness [μm]	Area weight [g m <sup>-2</sup> ]	Electrode density [g cm <sup>-3</sup> ]	Electrode porosity [%]
HC-A	93.3 ± 0.7	83.9 ± 0.9	0.90 ± 0.01	52.0 ± 0.3
HC-B	93.0 ± 1.2	79.5 ± 1.1	0.85 ± 0.01	56.8 ± 0.3
HC-C	93.8 ± 1.2	78.4 ± 1.4	0.84 ± 0.01	57.5 ± 0.6
Graphite	93.6 ± 0.9	82.6 ± 0.4	0.88 ± 0.01	58.7 ± 0.2

The influence of the particle size of the different HC on the electrodes properties is shown in **Table 2** as a comparison of the area weights of the coating, electrode densities, and electrode porosity. For this purpose, the same dry film thicknesses were set. The geometric porosity was determined using the area weight, density of the dry mixture, and dry film thickness. The data given for HC is averaged over the various electrodes investigated in this study for different drying rates (see Section 4.2). **Table 2** also shows the properties of a graphite anode with the same thickness.

As the particle size increases, the electrode porosity increases and does not change significantly by drying with increasing drying rate (Figure S4 and S5, Supporting Information). To get a visual impression of the microstructure of HC electrodes, cross-sectional SEM images are shown in **Figure 3**. For comparison, a SEM image of a graphite electrode is shown in Figure S1, Supporting Information.

The different particle sizes result in clear differences in the porosity (**Table 2**) and pore sizes in the electrodes. The corresponding pore size distributions are shown in **Figure 4**.

With increasing particle size, the dominant pore size of the electrodes increases (HC-A  $x_{50} = 3.7 \mu\text{m}$  corresponds to  $d_{\text{pore,peak}} = 0.6 \mu\text{m}$ , HC-B  $x_{50} = 5.0 \mu\text{m}$  to  $d_{\text{pore,peak}} = 1.1 \mu\text{m}$ , and HC-C  $x_{50} = 9.4 \mu\text{m}$  to  $d_{\text{pore,peak}} = 2 \mu\text{m}$ ). The changes of the pore size distribution of HC-A and HC-C (smallest and largest particle size) with increasing drying rate were also investigated. In Figure S5, Supporting Information, it can be seen that the drying rate has no influence on the pore size distribution. A comparison between the porosity determined according to the coating weight, the thickness, and the densities and the porosity measured by Hg intrusion is included in the Supporting Information.

### 2.4. Adhesion: Influence of Drying Rate and Film Temperature

In this study, the adhesion force (measured by 90° peel tests) of HC electrodes is investigated for increasing drying rates and film temperature, since the adhesion force provides an indirect measure for the binder content near the separator and characterizes the mechanical properties of the electrodes.<sup>[15,16,18,24,26]</sup> Section 4.3 provides information on determining of the adhesion force. The objective is to indicate the behavior of HC slurries in comparison to graphite from the literature at increased production rate during electrode processing.

The drying rate is adjusted in the range between  $0.75$  and  $9 \text{ g m}^{-2} \text{ s}^{-1}$ . For an average coating weight of about  $81 \text{ g m}^{-2}$

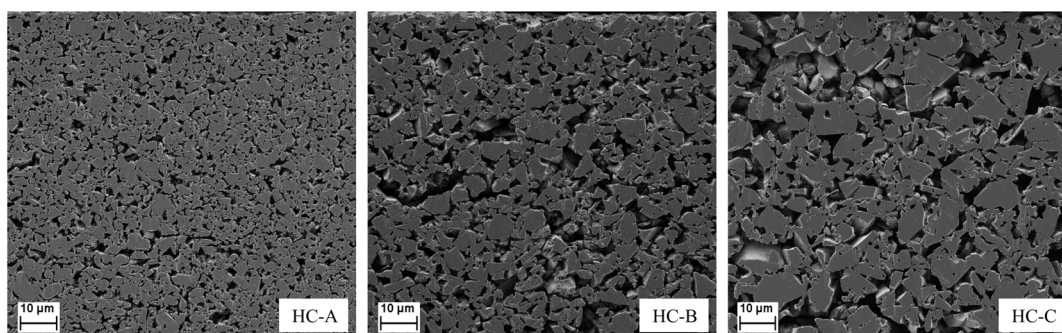


**Figure 3.** SEM cross-sectional images of dried HC electrodes (noncalendered). It can be clearly seen that the pore size between the particles increases with increasing particle size. The electrode density decreases and the porosity increases with increasing particle size. All electrodes were produced with the same composition, solid content, identical mixing procedure and with the same drying conditions ( $0.75 \text{ g m}^{-2} \text{ s}^{-1}$ ). In Figure S1, Supporting Information, an SEM image of a graphite electrode is shown for comparison.

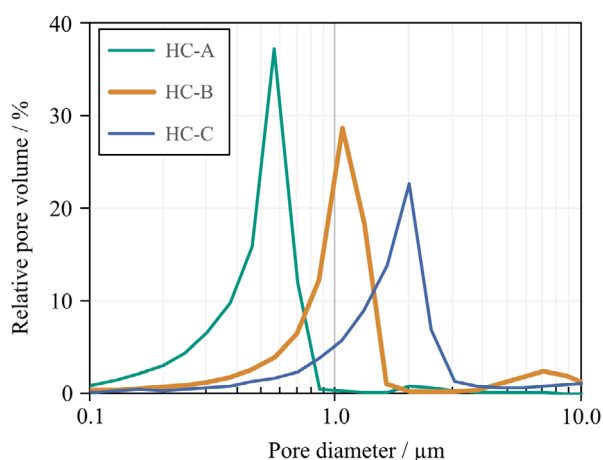


**Figure 4.** Pore size distribution measured by mercury (Hg) intrusion of the electrodes for the three investigated HC active materials. The HC-A electrodes are dominated by pores at  $0.6 \mu\text{m}$ , HC-B at  $1.1 \mu\text{m}$ , and HC-C at  $2 \mu\text{m}$ .

for the dry HC electrodes, the drying time can be reduced from 142 s to only 12 s in the drying rate range investigated, assuming drying kinetics controlled by gas phase only. Table 2 provides detailed information on the electrode thickness, coating weight, and porosity of the electrodes of the different materials.

To compare the sensitivity of the HC and graphite anodes for binder migration, the adhesion forces of HC-C from this study and graphite electrodes from the literature are compared and discussed first. The electrodes are compared with the same area capacity. The graphite anodes have an area capacity of  $2.2 \text{ mAh cm}^{-2}$  with a dry film thickness of  $\approx 75 \mu\text{m}$ .<sup>[18]</sup> With the coating weight of the HC electrodes and an assumed practical specific capacity of about  $300 \text{ mAh g}^{-1}$  <sup>[1,41]</sup> ( $\approx 200\text{--}400 \text{ mAh g}^{-1}$ ),<sup>[1,42,43]</sup> the average area capacity for the investigated HC electrodes is also  $2.2\text{--}2.3 \text{ mAh cm}^{-2}$ .

The adhesion forces were measured by  $90^\circ$  peel tests and are normalized to the respective adhesion force at the lowest drying rate investigated. Reference adhesion forces for a lower drying rate of  $0.75 \text{ g m}^{-2} \text{ s}^{-1}$  are  $9.41 \pm 0.17 \text{ N m}^{-1}$  for HC-C ( $93.8 \pm 1.2 \mu\text{m}$ ) and  $18.2 \text{ N m}^{-1}$  for graphite ( $75 \mu\text{m}$ ).<sup>[18]</sup> For an

equal dry film thickness of  $93.6 \pm 0.9 \mu\text{m}$ , a graphite anode has a reference adhesion force of  $14.5 \pm 0.4 \text{ N m}^{-1}$  with the same preparation methods presented in this study. More binder could be available for adhesion to the current collector due to the lower specific surface area of graphite, thus resulting in increased adhesion force. However, the adhesion might be affected differently by drying conditions. Hence, Figure 5 shows the normalized adhesion force as a function of the drying rate at different drying temperatures (heat transfer coefficients) for the HC-C and graphite<sup>[18]</sup> electrodes (see Section 4.2).

In the drying rate range investigated, the HC-C and graphite electrodes show a decreasing adhesion force. The trend of a decreasing adhesion force with increasing drying rate can be explained by an increased capillary transport during pore emptying and the associated transport of the SBR binder, which mainly is responsible for adhesion. This leads to a depletion of the SBR binder near the substrate and a lowered adhesion force.

It can be seen that the decrease in adhesion force is more pronounced for graphite electrodes than for HC-C electrodes, which results in an equal adhesion force for the HC-C and graphite electrodes of  $\approx 6 \text{ N m}^{-1}$  at a set heat transfer coefficient of  $35 \text{ W m}^{-2} \text{ K}^{-1}$  and an adhesion force of  $\approx 4 \text{ N m}^{-1}$  at  $80 \text{ W m}^{-2} \text{ K}^{-1}$  for the maximum drying rate investigated. For moderate drying rates, even no negative influence of the drying rate on the adhesion force can be observed for HC-C electrodes (Figure 5, left). For a decrease in the adhesion force of HC-C electrodes, a more intense capillary transport by an increased drying rate may be required to cause binder migration.

As another effect, the film temperature plays a role in the microstructure formation, that is yet not fully understood. In Figure 5 (left) and (right), the film temperature during drying differs to maintain a constant drying rate for an increasing heat transfer coefficient (Section 4). For the experiments in this work, the film temperatures differ by  $12 \pm 3^\circ \text{C}$  at the same drying rate for the two different heat transfer coefficients. For both materials, it can be seen that at comparatively lower film temperatures (Figure 5, right), the adhesion force is lower at the same drying rate as in Figure 5 (left). This confirms the findings from the literature that a higher film temperature at the same drying rate (lower heat transfer coefficient) is generally beneficial for the

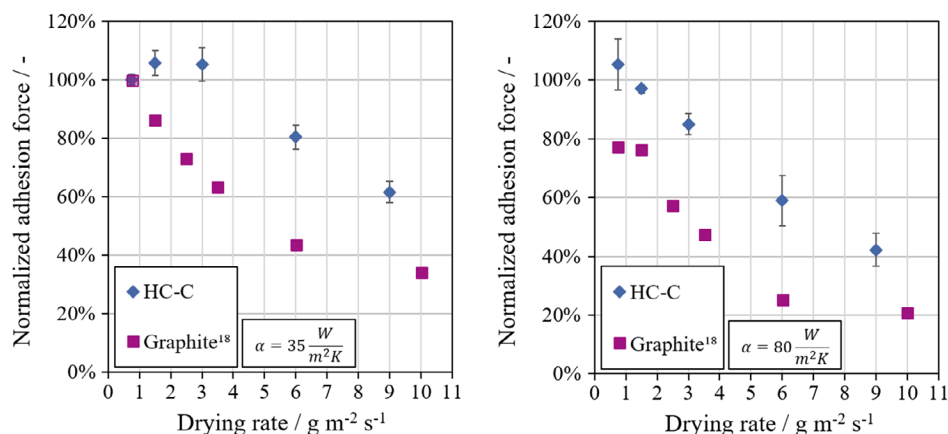


**Figure 5.** Adhesion forces (normalized to reference adhesion) of noncalendered HC-C and graphite anodes as a function of drying rate at two different heat transfer coefficients of  $35 \text{ W m}^{-2} \text{ K}^{-1}$  (left) and  $80 \text{ W m}^{-2} \text{ K}^{-1}$  (right). Drying rate is varied via the isothermal drying temperature (see Experimental Section). The data for the graphite electrodes is taken from the literature.<sup>[18]</sup> The reference adhesion for HC-C is  $9.41 \pm 0.17 \text{ N m}^{-1}$  and for graphite  $18.2 \text{ N m}^{-1}$ .

adhesion force of the electrodes.<sup>[18]</sup> The temperature effect is also discussed in the literature on water-based graphite anodes dried using near-infrared radiation (NIR).<sup>[44]</sup> As described in the literature, a higher temperature could lead to more and increased attraction between the CMC (and SBR) and the active material during drying.<sup>[16]</sup> Thus the role of the film temperature in binder migration may be explained by temperature-dependent interactions between CMC/SBR and particles during drying, highlighting the significance of interactions between the slurries' components.

In addition to the film temperature, the interaction of CMC/SBR depending on the particles can influence the drying behavior. Reduced or no binder migration has also been observed in the literature for the drying of graphite anode slurry derived from mixing with a kneader and when using smaller spherical graphite particles.<sup>[16]</sup> Herein, it is hypothesized that a stronger fixation of the CMC to the particles is responsible for the mitigation of binder migration. This may be reached due to a different surface chemistry, smaller particle size, or better deagglomeration of the conductive carbon black (due to higher-energy input during mixing). Assuming that the SBR binder is fixed to stationary CMC, this would reduce the mobile fraction of SBR binder, resulting in less pronounced binder migration during drying.<sup>[16]</sup>

It is hypothesized that the lower binder migration in the HC-C electrodes is due to a stronger fixation of more CMC/SBR to the smaller-sized particles of HC with a higher surface area compared to the same mass of graphite. If the capillary transport as the driving force for binder migration is large enough, the SBR binder still can be carried along in HC-C electrodes.

For a further reduction of the particle size, a further reduction of the mobile binder fraction is expected as well as a reproduced positive effect of a higher film temperature. From the rheological investigation, it has already been shown that the use of HC-A and HC-B leads to a gel-like network of CMC and particles, which supports the hypothesis regarding interactions in the slurries. To investigate the hypothesis that a reduction in particle size

leads to a reduction in the mobile binder fraction, and thus, lower binder migration, **Figure 6** shows a comparison of the adhesion force of HC-C electrodes compared to HC-A and HC-B with smaller particle size.

For an increasing drying rate up to  $3.0 \text{ g m}^{-2} \text{ s}^{-1}$  at the lower heat transfer coefficient, the HC electrodes show a constant or even increased adhesion force (Figure 6, left). For HC-A and HC-B electrodes, higher drying rates first lead to an increase and subsequently to a constant adhesion force level. This suggests that for HC-A and HC-B, the migration of the SBR binder is not present or the mechanism is superimposed by some other effect. Above a drying rate of  $6 \text{ g m}^{-2} \text{ s}^{-1}$ , this effect seems to be equalized. Further increase of temperature or drying rate leads to approximately the same adhesion force.

Generally, SBR binder is drawn away by capillary transport from the interface of current collector and coating. The behavior of the HC-A and HC-B electrode indicates that more CMC/SBR is fixed more strongly to the smaller particles and thus less mobile binder is available. In addition, a further increase in drying rate by increasing the drying temperature even has the effect of enhancing the adhesion to the current collector. In this case for HC-A and HC-B, the mobile binder fraction during capillary transport seems to decrease for higher drying rates (due to higher film temperatures) and to additionally participate to the adhesion. Once there is no longer a mobile binder available that is prevented by the CMC from migrating, adhesion cannot increase any further with increasing drying temperature. For a slurry in which the fixation of the CMC network is weaker, this would not be the case since a higher proportion of mobile binder is present, which can be moved by a higher drying rate and capillary transport. Additionally, in such system, CMC may possibly migrate through the capillary transport.

The relative share of mobile binder changes, depending on the particles, the drying conditions, and the driving force of the binder migration. As described in the literature, the higher temperature could lead to increased attraction of the CMC (and SBR) to the active material during drying.<sup>[16]</sup>

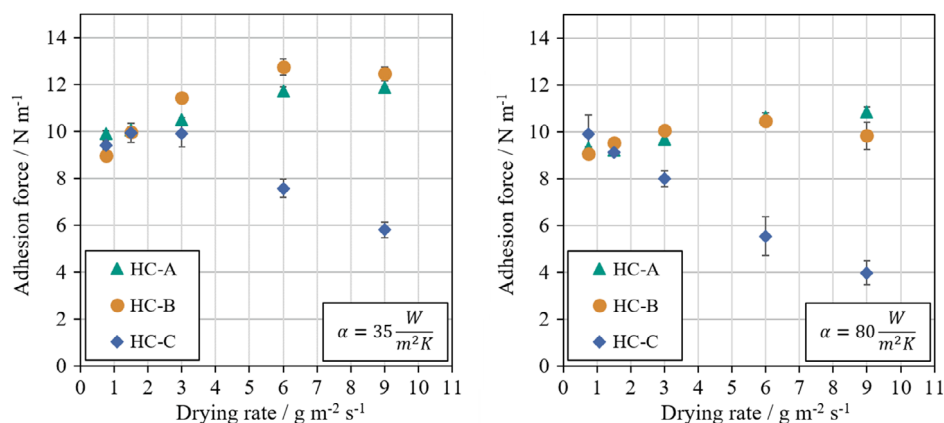


**Figure 6.** Adhesion force (noncalendered) of HC anodes as a function of drying rate at a constant heat transfer coefficient of  $35\ W\ m^{-2}\ K^{-1}$  (left) and  $80\ W\ m^{-2}\ K^{-1}$  (right). The drying rate is varied via the isothermal drying temperature (see Experimental Section). All HC show at least a constant adhesion force for moderate drying rates. The comparatively smaller HC-A and HC-B particles show an increasing or constant adhesion force over nearly the entire drying rate range (142–12 s drying time).

Since the adhesion force of the HC-C electrodes only decreases above a certain drying rate ( $>3\ g\ m^{-2}\ s^{-1}$ ), this suggests that a reduction in binder transport is also caused thereby, for example, the described binding of the CMC/SBR to the particles. This cannot be suspected from the rheological investigation alone, if a gel-like behavior should be responsible for a suppression of binder migration. However, it cannot be ruled out that a HC-C slurry also forms a gel-like behavior during drying due to the reduction of the water content. It can be hypothesized that a slurry that exhibits gel-like behavior prior to entering capillary transport during drying could exhibit reduced binder migration. This is not investigated further in this study.

During drying with a higher heat transfer coefficient (Figure 6, right), and thus, a larger forced convection, it can be seen that all investigated HC electrodes show the same trends with increasing drying rate as in the case of a lower heat transfer coefficient. However, almost all electrodes have a lower adhesion force compared to a lower heat transfer coefficient, though the overall drying rate is the same. For HC-A and HC-B the increase of adhesion force with the film temperature is also less pronounced for the higher heat transfer coefficient and thus lower film temperatures. This supports the hypothesis that, in addition to the drying rate and capillary transport, the film temperature has a crucial role in binder migration and the bridging of the CMC network with the particles at the start of capillary action. To exclude that a higher film temperature leads to an adhesion, increasing annealing of the electrodes, the electrodes HC-A and HC-C were treated with different annealing temperatures after drying and the adhesion force was determined (Figure S6, Supporting Information). For the HC-A electrodes, an annealing temperature higher than  $100\ ^\circ C$  leads to an increase in adhesion. The maximum film temperature in this study is  $70\ ^\circ C$ .

As the adhesion to the current collector is only an indirect measure for a homogenous binder distribution over the electrode cross section, the impact of drying will be further investigated by impedance spectroscopy in Section 2.5 for HC-A compared to HC-C electrodes at increased drying rates.

## 2.5. Binder Migration and Ionic Transport Resistance

The adhesion force provides an indirect measure for the binder migration that can only provide information about the interaction near the current collector. A more holistic prediction about the binder distribution after drying can be made by impedance spectroscopy under blocking conditions, which has been investigated via simulations and experimentally in the literature for graphite anodes.<sup>[27,45]</sup> Tetrabutylammonium perchlorate TBAClO<sub>4</sub> in EC:DMC (1:1 by volume) was used as a blocking electrolyte. This electrolyte contains no ions that can be intercalated in the active material. Further information on the measurement is given in Section 4.4. Since the HC-A and HC-C electrodes show inverse behavior in terms of adhesion with increasing drying rate, these electrodes were investigated and are discussed in this section. To show the effects of binder migration on the impedance spectroscopy measurement, Figure 7 exemplarily shows the Nyquist plots for HC-A and HC-C for the lowest ( $0.75\ g\ m^{-2}\ s^{-1}$ ) and highest ( $9\ g\ m^{-2}\ s^{-1}$ ) drying rates studied.

Consistent with the literature,<sup>[27,46]</sup> the midfrequency region for HC-C electrodes is extended at a drying rate of  $9\ g\ m^{-2}\ s^{-1}$  compared to  $0.75\ g\ m^{-2}\ s^{-1}$ . The binder gradient along the electrode thickness with increasing drying rate would be consistent with an increase in the midfrequency region and extended curvature for binder migration with increasing drying rate found in the literature for graphite anodes with PVDF binder.<sup>[27]</sup> The impedance measurements from Figure 7 were fit with a transmission line model (TLM) to obtain the ionic transport resistance  $R_{ion}$ . The TLM represents the diffusion of ions in the electrolyte in the pore structure of the electrode. The ionic transport resistance for the HC-A electrodes is almost unchanged from 268 to 249 Ohm (7% reduction) at the highest drying rate compared to the lowest drying rate. The HC-C electrodes have a higher ionic transport resistance of 605 Ohm for the lowest drying rate and the ionic transport resistance increases significantly to 802 Ohm (33% increase) for the higher drying rate. For graphite anodes with PVDF, this increase of the ionic

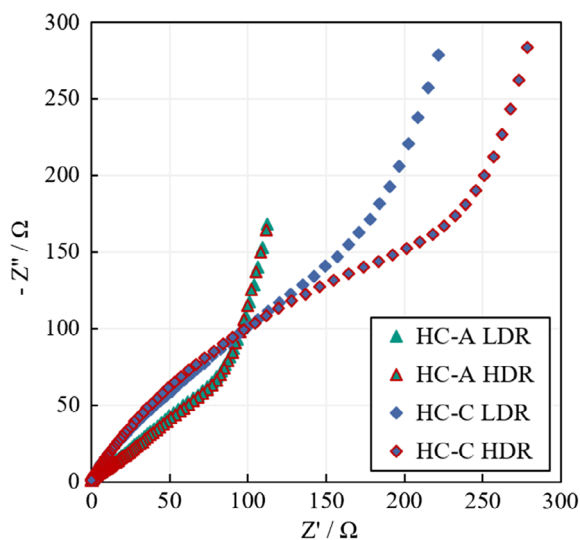


**Figure 7.** Nyquist plots of symmetric cell configuration under blocking conditions of HC-A and HC-C electrodes for the lowest drying rate (LDR  $0.75 \text{ g m}^{-2} \text{ s}^{-1}$ ) and the highest drying rate (HDR  $9 \text{ g m}^{-2} \text{ s}^{-1}$ ) investigated (noncalendered electrodes). The measurements were performed with 10 mV perturbation and a frequency range from 200 kHz to 100 mHz. The HC-C electrode shows higher ionic transport resistances compared to the HC-A electrode and an increase of the ionic transport resistance at the higher drying rate.

resistance with increase in binder migration has also been found in the literature.<sup>[27]</sup>

In order to correlate the impedance spectroscopy with the adhesion force measurements from Section 2.4, the ionic transport resistances for HC-A and HC-C electrodes were determined over the entire range of the drying rate studied and compared by the electrical tortuosity calculated using Equation (2) (Section 4.4). The tortuosity is shown as a function of the drying rate and is compared to the adhesion force measurements in Figure 8.

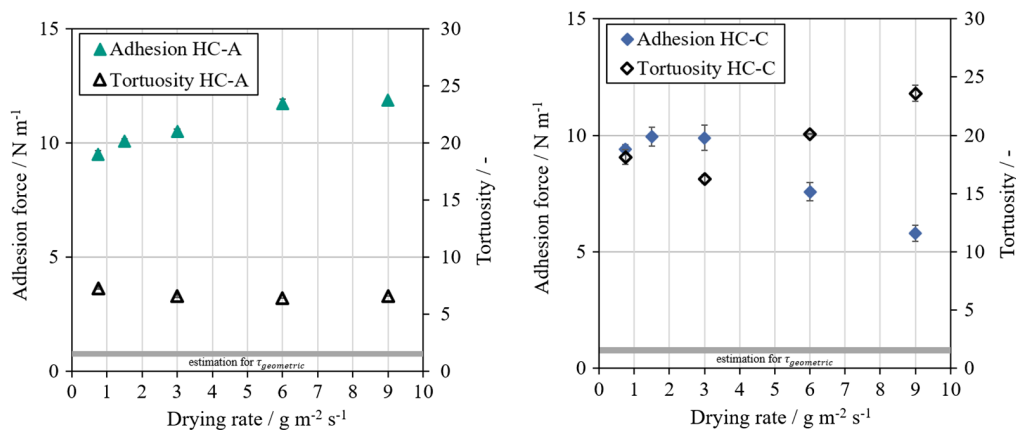


**Figure 8.** Electrical tortuosity from impedance spectroscopy measurements of HC-A (left) and HC-C (right) electrodes as a function of the drying rate in comparison with the adhesion force of the electrodes. The tortuosity curve represents inversely the same trends as the adhesion force measurements for both HC. For HC-A and HC-C, the electrical tortuosity leads to by far higher values compared to values estimated from heat or mass transfer measurements and analytical estimation according to, for example, Bruggeman ( $\tau = \varepsilon^\gamma$  with  $\gamma = -0.5$ )<sup>[55]</sup> and Zehner–Bauer–Schlünder ( $\tau = \varepsilon / (1 - (1 - \varepsilon)^{-1.5})$ )<sup>[49,50]</sup> for the geometrical tortuosity ( $\tau_{\text{geometric}}$ ).

The electrical tortuosity from impedance measurements with the HC-A and HC-C electrodes shows significantly higher values compared to the estimates for the geometrical tortuosity. In addition, the measured electrical tortuosity increases for the HC-C electrodes at higher drying rates, while the geometrical tortuosity according to Bruggeman or Zehner–Bauer–Schlünder is only a function of porosity (at least according to most literature correlations) and the electrode porosity does not change with the drying rate (Figure S4, Supporting Information). A reason for the observed difference is that the geometric porosity describes only the pure change in path length. It has been shown in the literature that the carbon black–binder–domain (CBD) between the active material particles is the most likely reason for underestimating the electrical tortuosity of porous electrodes from only the geometrical structure.<sup>[45–47]</sup> According to Equation (2), only the ionic transport resistance in the electrode changes for the calculation of the electrical tortuosity, with the same electrode geometry. For example, changing the binder distribution, the amount of binder, or the type of binder changes the ionic transport resistance or the distribution of ionic transport resistances in the electrode and thus, the electrical tortuosity.<sup>[27,45,48]</sup> From these results, it can be concluded that it is necessary to distinguish between electrical tortuosity by electrical impedance spectroscopy for describing the ion transport in porous electrodes and geometrical tortuosity for heat and mass transfer, where only the change in path length is considered.<sup>[49–53]</sup>

The electrical tortuosity of the HC-A electrodes (Figure 8, left) decreases slightly at higher drying rate and is lower compared to HC-C electrodes (Figure 8, right). Since the electrical tortuosity does not increase for increasing drying rate, it can be assumed that the statements by the adhesion force measurement can be confirmed and that these HC-A electrodes have a lower ionic transport resistance due to the suppression of the binder migration. The binder distribution appears to remain constant as the drying rate increases. The result that the HC-A electrodes have a lower tortuosity compared to the HC-C electrodes can be attributed to the higher number of pores. The HC-A electrodes with

the smaller pore sizes (Figure 4) enable a larger number of possible transport paths for the ions to move through the electrode.

The HC-C electrodes show a higher electrical tortuosity at higher drying rate and thus, a strong influence of binder migration. The tortuosity curve corresponds to the inverse curve of the adhesive force measurement. In particular, the range between 0.75 and 3 g m<sup>-2</sup> s<sup>-1</sup> is also confirmed by the impedance measurement. At moderate drying rates, an increase in adhesion force and a decrease in electrical tortuosity are observed first. Drying rates higher than 3 g m<sup>-2</sup> s<sup>-1</sup> lead to a strong increase in tortuosity of about 30% compared to 0.75 g m<sup>-2</sup> s<sup>-1</sup> as well as a strong reduction in adhesion force (about 40%).

The magnitude of the electrical tortuosity for both HC electrodes is consistent with tortuosity determinations using electrochemical impedance spectroscopy (EIS) on graphite anodes with CMC/SBR from the literature and may be lowered, for example, by reducing the binder content.<sup>[45]</sup> A lower binder content or electrical tortuosity could have a positive effect on the electrochemical performance in this context, but is not further investigated in this study.

### 3. Conclusion

In this study, the electrode processing of different HC particles for sodium-ion batteries at different drying rates was investigated and comparatively analyzed with the drying behavior of graphite anodes from the literature. It is found that analogous effects occur with HC anodes for SIB with the processing of graphite anodes for LIB. However, the interaction of the particles with the aqueous binder system CMC/SBR changes the properties of the slurry and especially the behavior during the drying and microstructure formation.

With the same formulation of all slurries, a viscosity comparable to a graphite anode's slurry with nonspherical particles was achieved, especially for higher shear rates. It can be assumed that the slurries are suitable for typical coating processes and coating speeds for battery applications.

The study shows that the HC electrodes exhibit a constant or slightly increased adhesion force at moderate drying rates. Up to a drying rate of 3 g m<sup>-2</sup> s<sup>-1</sup> (drying time of 36 s), none of the HC materials show a decrease in adhesion force, as might have been suspected from the literature for different material systems. At very high drying rates (12 s drying time), the adhesion forces increase by 25–39% of the comparatively smaller particle size of HC-A and HC-B electrodes compared to their reference adhesion force at low drying rate. This can be attributed to stronger fixation of the CMC/SBR network to these particles, as also found for graphite in the literature. It was found that the formation of the CMC/SBR network must be different for the various HC particles. An increased drying rate leads to a more intense capillary transport, which is considered to be the driving force for binder migration. Depending on the strength of the CMC/SBR network, binder migration may still occur. This has to be further investigated by the aimed enforcing of slurry properties and the investigation of microstructure formation for increasing drying rate.

Another effect is the temperature during drying of the electrodes. Increasing the heat transfer coefficient, which is a measure of the convection in the gas phase, results in a lower isothermal

drying temperature at the same drying rate compared to a lower heat transfer coefficient. Since the adhesion force is higher at comparatively lower heat transfer coefficient, and thus, higher film temperature, this indicates that higher temperature supports CMC crosslinking and mitigates binder migration. It was excluded in this study that a higher film temperature could lead to an annealing effect.

By impedance measurements under blocking conditions, it was shown that the trends of the binder migration or the suppression of binder migration can also be confirmed by the ionic transport resistance or the electrical tortuosity in the electrodes. In particular, it is shown that the ionic transport resistance of HC-A electrodes decreased slightly at higher drying rate as well as the adhesion force increased slightly. This suggests that the binder distribution remained homogeneously distributed through the higher drying rate.

The study shows that processing of HC shows many parallels with the present manufacturing methods and equipment for mixing, coating, and drying of LIB. However, for new materials in SIB, investigations with selected electrode compositions are necessary with regard to the behavior of the adhesion force and other effects of binder migration on the electrode properties.

Multilayer architectures could be investigated for further studies to enhance the absolute adhesion force of HC electrodes at very high production speeds. A multilayer structure of two different HC particles with different sizes and an impressed binder gradient could increase the adhesion force and lead to lower ionic transport resistances. In addition, the overall surface area of the active material in the electrode can be reduced, resulting in positive effects with regard to SEI formation. In further studies the effect of the viscosity on the pore emptying mechanism needs to be clarified as an explanation for higher adhesion force at comparatively higher viscosity. Besides that, increased production speeds using radiation-based drying methods should be investigated. Thereby, a higher film temperature can be realized during drying and thus a higher adhesion force can be induced.

### 4. Experimental Section

**Material Characterization:** The specific surface areas were obtained by BET measurements using nitrogen adsorption gas (Gemini VII 2390, Micromeritics). The density of the materials was measured by helium pycnometry (AccuPyc 1330, Porotec).

**Mixing:** The slurries for HC-A, HC-B, HC-C (Kuranode Type II: 3, 5, and 9 μm, kuraray), and graphite (SMGA, Hitachi Chemical Co. Ltd., Japan) were mixed in a dissolver (Dispermat SN-10, VMA Getzmann GmbH Verfahrenstechnik, Germany). Carbon black (Super C65, Imerys) and HC powder were mixed in a dry mixing step for 10 min at 200 rpm. A 2 wt% CMC (Sunrose MAC500LC, Nippon Paper Industries, Japan) solution was added to 1/3 of the mixed particles and dispersed at 500 rpm for 10 min. The remaining particles were added in two equal steps and further dispersed. Further water was added for the final solid content. The slurries were then mixed for 45 min at 1500 rpm. The container was cooled and degassed in the process. In the final step, SBR (Zeon Europe GmbH, Japan) was added and the slurry was mixed for 10 min at 500 rpm. The composition was chosen so that the dry electrode has the composition in Table 3. The viscosity was measured by a rotation viscometer Physica MCR 101 (Anton Paar, Germany) with a plate-plate geometry (25 mm diameter) from 0.01 to 1.000 s<sup>-1</sup> at 25 °C.

**Electrode Coating and Drying:** The coating and drying of the HC and graphite slurries was carried out in a discontinuous process, as described

**Table 3.** Composition of dry electrodes.

Name	HC or graphite [wt%]	Carbon Black [wt%]	CMC [wt%]	SBR [wt%]	Solids [wt%]
HC-A, HC-B, HC-C, Graphite	93.00	1.40	1.87	3.73	43.00

by Baunach et al.<sup>[23]</sup> The 10  $\mu\text{m}$  copper current collector (Civen Metal Material Co. Ltd., China) was attached to a temperature-controlled plate via vacuum. The coating of the anode slurries was applied with a doctor blade ZUA 2000.60 (Zehntner) and subsequently the coating was run under the drying nozzles of an impingement dryer. For homogeneous drying, the plate was periodically moved under the dryer until the slurry was dry. The drying temperature and heat transfer coefficient were set independently to separate their respective effects. For all experiments, the drying rate was determined by the temperature of the heated plate and the heat transfer coefficient of the slot nozzle dryer, taking into account the dew point of the drying air. **Table 4** shows the drying rates, heat transfer coefficients, and the drying temperatures. Further information on the drying temperature and the drying rate is given in the literature.<sup>[15,18]</sup> The different heat transfer coefficients result in an average temperature difference of  $12 \pm 3$  °C for the same drying rate.

**Electrode Characterization:** The porosity was calculated from the area weight  $m_{\text{electrode}}$  divided by the layer thickness  $h_{\text{dry}}$  and the density (measured by helium pycnometry) of the dry mixture of the components  $\rho_{\text{dry mixture}}$ :

$$\epsilon_{\text{electrode}} = 1 - \frac{m_{\text{electrode}}}{\rho_{\text{dry mixture}} h_{\text{dry}}} \quad (1)$$

The pore size distribution of the electrodes was measured with a mercury intrusion porosimeter (Pascal 440 Evo, Thermo Scientific). The current collector was considered for the calculation of porosity as described in the literature.<sup>[46,54]</sup> For the SEM images, a field-emission scanning electron microscope (Zeiss Supra 55) from Carl Zeiss AG (Oberkochen, Germany) was used.

**Adhesion Force Measurements:** To determine the adhesion force between the current collector and the dried electrodes, a 90° peel test was carried out with a universal testing machine AMETEK LS1 (Lloyd Instruments Ltd., UK) and a 10 N load cell. All samples of the dried anodes were cut out with a width of 30 mm and attached with the coated side to an adhesive strip. The sample was pressed on with a weight of 10 kg to ensure uniform contact between the coating and the adhesive strip. The current collector foil was then peeled off the coating at a constant speed of

**Table 4.** Overview of the drying rate and the drying temperature with a constant heat transfer coefficient of  $35 \text{ W m}^{-2} \text{ K}^{-1}$  and  $80 \text{ W m}^{-2} \text{ K}^{-1}$ . The average dew point for the experiments was  $11 \pm 2$  °C.

Drying rate [ $\text{g m}^{-2} \text{ s}^{-1}$ ]	Heat transfer coefficient [ $\text{W m}^{-2} \text{ K}^{-1}$ ]	Drying film temperature [°C]
0.75	35	31
	80	23
1.50	35	40
	80	29
3.00	35	51
	80	38
6.00	35	63
	80	48
9.00	35	70
	80	55

600  $\text{mm min}^{-1}$  at a 90° angle using the testing machine. The resulting pull-off force was measured and divided by the sample width to obtain a line adhesion force.

**Impedance Spectroscopy Measurements:** The ionic resistance  $R_{\text{ion}}$  was measured in symmetric coin cells (CR2032) with one spacer for each electrode and two glass fiber separators (GF/C, Whatman) per cell. The cells were assembled in a glove box (MBraun). As electrolyte, 200  $\mu\text{L}$  of 10 mM tetrabutylammonium perchlorate TBAClO<sub>4</sub> in EC:DMC (1:1 by volume) was added. This blocking electrolyte did not contain ions that could be intercalated into the active material (blocking conditions). The conductivity of this electrolyte was  $\kappa = 0.3505 \pm 0.0011 \text{ mS cm}^{-1}$ . Electrodes and separators were punched out with a diameter of 1.6 cm corresponding to an area  $A = 2.01 \text{ cm}^2$ . EIS measurements were performed in a temperature-controlled chamber (BTZ-175, Espec) at 25 °C using a coin cell holder (Dual CR2032 Coin Cell Holder, Gamry Instruments) with a potentiostat (VSP-300, Biologic). The measuring parameters were 10 mV perturbation and a frequency range from 200 kHz to 100 mHz. The impedance measurements were fit in an EIS software (RelaxIS 3, rhd instruments) with a TLM to obtain the ionic transport resistance  $R_{\text{ion}}$ . The electrical tortuosity was calculated by Equation (2) with the dry film thickness  $h_{\text{dry}}$  and the porosity  $\epsilon$  of the electrode, as described by Landesfeind et al.<sup>[48]</sup>

$$\tau = \frac{R_{\text{ion}} A \kappa \epsilon}{2 h_{\text{dry}}} \quad (2)$$

## Supporting Information

Supporting Information is available from the Wiley Online Library or from the author.

## Acknowledgements

This work was funded by the Deutsche Forschungsgemeinschaft (DFG, German Research Foundation) under Germany's Excellence Strategy, EXC 2154, project number 390874152 (POLiS Cluster of Excellence), and contributes to the research performed at Center for Electrochemical Energy Storage Ulm Karlsruhe (CELEST).

Open Access funding enabled and organized by Projekt DEAL.

## Conflict of Interest

The authors declare no conflict of interest.

## Data Availability Statement

The data that support the findings of this study are available from the corresponding author upon reasonable request.

## Keywords

battery electrode processing, binder migration, electrode drying, lithium-ion batteries, postlithium batteries, sodium-ion batteries, tortuosity

Received: March 29, 2023

Revised: May 15, 2023

Published online:

[1] M.-M. Titirici, P. Adelhelm, Y.-S. Hu, in *Materials, Characterization, and Technology*. Vol 1, 2nd ed., Wiley-VCH, Weinheim 2023.

[2] P. K. Nayak, L. Yang, W. Brehm, P. Adelhelm, *Angew. Chem.* 2018, 57, 102.

- [3] N. Yabuuchi, K. Kubota, M. Dahbi, S. Komaba, *Chem. Rev.* **2014**, *114*, 11636.
- [4] D. Larcher, J.-M. Tarascon, *Nat. Chem.* **2015**, *7*, 19.
- [5] J. Peters, A. Peña Cruz, M. Weil, *Batteries* **2019**, *5*, 10.
- [6] H. Liu, M. Baumann, X. Dou, J. Klemens, L. Schneider, A.-K. Wurba, M. Häring, P. Scharfer, H. Ehrenberg, W. Schabel et al., *J. Energy Storage* **2022**, *56*, 105964.
- [7] Y. Liu, B. V. Merinov, W. A. Goddard, in *Proc. Natl. Acad. Sci. USA* **2016**, *113*, 3735.
- [8] L.-F. Zhao, Z. Hu, W.-H. Lai, Y. Tao, J. Peng, Z.-C. Miao, Y.-X. Wang, S.-L. Chou, H.-K. Liu, S.-X. Dou, *Adv. Energy Mater.* **2021**, *11*, 2002704.
- [9] B. Xiao, T. Rojo, X. Li, *ChemSusChem* **2019**, *12*, 133.
- [10] X. Dou, I. Hasa, D. Saurel, C. Vaalma, L. Wu, D. Buchholz, D. Bresser, S. Komaba, S. Passerini, *Mater. Today* **2019**, *23*, 87.
- [11] W. Zhang, F. Zhang, F. Ming, H. N. Alshareef, *EnergyChem* **2019**, *1*, 100012.
- [12] C. Vaalma, D. Buchholz, M. Weil, S. Passerini, *Nat. Rev. Mater.* **2018**, *3*, 18013.
- [13] N. Tapia-Ruiz, A. R. Armstrong, H. Alptekin, M. A. Amores, H. Au, J. Barker, R. Boston, W. R. Brant, J. M. Brittain, Y. Chen et al., *J. Phys. Energy* **2021**, *3*, 31503.
- [14] I. Hasa, S. Mariyappan, D. Saurel, P. Adelhelm, A. Y. Kuposov, C. Masquelier, L. Croguennec, M. Casas-Cabanas, *J. Power Sources* **2021**, *482*, 228872.
- [15] J. Klemens, L. Schneider, E. C. Herbst, N. Bohn, M. Müller, W. Bauer, P. Scharfer, W. Schabel, *Energy Technol.* **2022**, *10*, 2100985.
- [16] J. Kumberg, W. Bauer, J. Schmatz, R. Diehm, M. Tönsmann, M. Müller, K. Ly, P. Scharfer, W. Schabel, *Energy Technol.* **2021**, *9*, 2100367.
- [17] S. Jaiser, L. Funk, M. Baunach, P. Scharfer, W. Schabel, *J. Colloid Interface Sci.* **2017**, *494*, 22.
- [18] J. Kumberg, M. Müller, R. Diehm, S. Spiegel, C. Wachsmann, W. Bauer, P. Scharfer, W. Schabel, *Energy Technol.* **2019**, *7*, 1900722.
- [19] L. Mauler, F. Duffner, J. Leker, *Appl. Energy* **2021**, *286*, 116499.
- [20] S. Jaiser, J. Kumberg, J. Klaver, J. L. Urai, W. Schabel, J. Schmatz, P. Scharfer, *J. Power Sources* **2017**, *345*, 97.
- [21] S. Jaiser, M. Müller, M. Baunach, W. Bauer, P. Scharfer, W. Schabel, *J. Power Sources* **2016**, *318*, 210.
- [22] B. Westphal, H. Bockholt, T. Gunther, W. Haselrieder, A. Kwade, *ECS Trans.* **2015**, *64*, 57.
- [23] M. Baunach, S. Jaiser, S. Schmelzle, H. Nirschl, P. Scharfer, W. Schabel, *Dry. Technol.* **2016**, *34*, 462.
- [24] R. Diehm, J. Kumberg, C. Dörrer, M. Müller, W. Bauer, P. Scharfer, W. Schabel, *Energy Technol.* **2020**, *8*, 1901251.
- [25] R. Diehm, M. Müller, D. Burger, J. Kumberg, S. Spiegel, W. Bauer, P. Scharfer, W. Schabel, *Energy Technol.* **2020**, *8*, 2000259.
- [26] J. Kumberg, M. Baunach, J. C. Eser, A. Altvater, P. Scharfer, W. Schabel, *Energy Technol.* **2021**, *9*, 2100013.
- [27] R. Morasch, J. Landesfeind, B. Suthar, H. A. Gasteiger, *J. Electrochem. Soc.* **2018**, *165*, A3459.
- [28] B. G. Westphal, A. Kwade, *J. Energy Storage* **2018**, *18*, 509.
- [29] H. Buqa, M. Holzapfel, F. Krumeich, C. Veit, P. Novák, *J. Power Sources* **2006**, *161*, 617.
- [30] F. Jeschull, D. Brandell, M. Wohlfahrt-Mehrens, M. Memm, *Energy Technol.* **2017**, *5*, 2108.
- [31] J. Drogenik, M. Gaberscek, R. Dominko, F. W. Poulsen, M. Mogensen, S. Pejovnik, J. Jamnik, *Electrochim. Acta* **2003**, *48*, 883.
- [32] R. Gordon, R. Orias, N. Willenbacher, *J. Mater. Sci.* **2020**, *55*, 15867.
- [33] W. J. Chang, G. H. Lee, Y. J. Cheon, J. T. Kim, S. I. Lee, J. Kim, M. Kim, W. I. Park, Y. J. Lee, *ACS Appl. Mater. Interfaces* **2019**, *11*, 41330.
- [34] S. Lim, S. Kim, K. H. Ahn, S. J. Lee, *J. Power Sources* **2015**, *299*, 221.
- [35] T. Mezger, in *Das Rheologie Handbuch. Für Anwender Von Rotations- Und Oszillations-Rheometern*, Vinzentz Network, Hannover **2016**.
- [36] W. B. Hawley, J. Li, *J. Energy Storage* **2019**, *25*, 100862.
- [37] S. Spiegel, A. Hoffmann, J. Klemens, P. Scharfer, W. Schabel, *Energy Technol.* **2022**, *11*, 2200684.
- [38] S. Spiegel, T. Heckmann, A. Altvater, R. Diehm, P. Scharfer, W. Schabel, *J. Coat Technol. Res.* **2022**, *19*, 121.
- [39] A. Hoffmann, S. Spiegel, T. Heckmann, P. Scharfer, W. Schabel, *J. Coat Technol. Res.* **2023**, *20*, 3.
- [40] R. Diehm, H. Weinmann, J. Kumberg, M. Schmitt, J. Fleischer, P. Scharfer, W. Schabel, *Energy Technol.* **2020**, *8*, 1900137.
- [41] F. Linsenmann, D. Pritzl, H. A. Gasteiger, *J. Electrochem. Soc.* **2021**, *168*, 10506.
- [42] B. Xiao, F. A. Soto, M. Gu, K. S. Han, J. Song, H. Wang, M. H. Engelhard, V. Murugesan, K. T. Mueller, D. Reed et al., *Adv. Energy Mater.* **2018**, *8*, 1801441.
- [43] S. Wu, X. Lu, K. Zhang, J. Xu, Z. Sun, *Batteries Supercaps* **2023**, *6*, e202200427.
- [44] A. Altvater, T. Heckmann, J. C. Eser, S. Spiegel, P. Scharfer, W. Schabel, *Energy Technol.* **2022**, 2200785.
- [45] J. Landesfeind, A. Eldiven, H. A. Gasteiger, *J. Electrochem. Soc.* **2018**, *165*, A1122.
- [46] L. Schneider, J. Klemens, E. C. Herbst, M. Müller, P. Scharfer, W. Schabel, W. Bauer, H. Ehrenberg, *J. Electrochem. Soc.* **2022**, *169*, 100553.
- [47] J. Landesfeind, M. Ebner, A. Eldiven, V. Wood, H. A. Gasteiger, *J. Electrochem. Soc.* **2018**, *165*, A469.
- [48] J. Landesfeind, J. Hattendorff, A. Ehrl, W. A. Wall, H. A. Gasteiger, *J. Electrochem. Soc.* **2016**, *163*, A1373.
- [49] P. Zehner, E. U. Schlünder, *Chem. Ingen. Tech.* **1970**, *42*, 933.
- [50] P. Zehner, E. U. Schlünder, *Chem. Ingen. Tech.* **1973**, *45*, 272.
- [51] J. C. Eser, B. Deichmann, T. Wirsching, L. Merklein, M. Müller, P. Scharfer, W. Schabel, *Dry. Technol.* **2022**, *40*, 1130.
- [52] D. Oehler, P. Seegert, T. Wetzel, *Energy Technol.* **2021**, *9*, 2000574.
- [53] T. Heckmann, J. C. Eser, A. Altvater, N. Streller, P. Scharfer, W. Schabel, *Energy Technol.* **2022**, *11*, 2200859.
- [54] L. Froboese, P. Titscher, B. Westphal, W. Haselrieder, A. Kwade, *Mater. Character.* **2017**, *133*, 102.
- [55] D. A. G. Bruggeman, *Ann. Phys.* **1935**, *416*, 636.